arXiv:0707.0693v1 [astro-ph] 4 Jul 2007

Accepted for Publication in ApJ

Feedback in the local LBG Analog Haro 11 as probed by far-UV and X-ray observations

J. P. Grimes[1], T. Heckman[1], D. Strickland[1], W. V. Dixon[1], K. Sembach[2], R. Overzier[1], C. Hoopes[1], A. Aloisi[2], and A. Ptak[1]

ABSTRACT

We have re-analyzed *FUSE* data and obtained new *Chandra* observations of Haro 11, a local ($\mathrm{D_L}$=88 Mpc) UV luminous galaxy. Haro 11 has a similar far-UV luminosity ($10^{10.3}\,\mathrm{L}_\odot$), UV surface brightness ($10^{9.4}\,\mathrm{L}_\odot\,\mathrm{kpc}^{-2}$), SFR, and metallicity to that observed in Lyman Break Galaxies (LBGs). We show that Haro 11 has extended, soft thermal (kT ~ 0.68 keV) X-ray emission with a luminosity and size which scales with the physical properties (e.g. SFR, stellar mass) of the host galaxy. An enhanced α/Fe ratio of ~ 4 relative to solar abundance suggests significant supernovae enrichment. These results are consistent with the X-ray emission being produced in a shock between a supernovae driven outflow and the ambient material. The FUV spectra show strong absorption lines similar to those observed in LBG spectra. A blueshifted absorption component is identified as a wind outflowing at $\sim 200-280$ km s^{-1}. O VI$\lambda\lambda$1032,1038 emission, the dominant cooling mechanism for coronal gas at T $\sim 10^{5.5}$K is also observed. If associated with the outflow, the luminosity of the O VI emission suggests that $\lesssim 20\%$ of the total mechanical energy from the supernovae and solar winds is being radiated away. This implies that radiative cooling through O VI is not significantly inhibiting the growth of the outflowing gas. In contradiction to the findings of Bergvall et al. (2006), we find no convincing evidence of Lyman continuum leakage in Haro 11. We conclude that the wind has not created a "tunnel" allowing the escape of a significant fraction of Lyman continuum photons and place a limit on the escape fraction of $\mathrm{f_{esc}} \lesssim 2\%$. Overall, both Haro 11 and a previously observed LBG analogue VV 114, provide an invaluable insight into the X-ray and FUV properties of high redshift LBGs.

---

[1] Center for Astrophysical Sciences, Johns Hopkins University, 3400 N. Charles St, Baltimore, MD 21218; jgrimes@pha.jhu.edu, heckman@pha.jhu.edu, dks@pha.jhu.edu,ptak@pha.jhu.edu

[2] Space Telescope Science Institute, 3700 San Martin Drive, Baltimore, MD, 21218; sembach@stsci.edu,aloisi@stsci.edu

Subject headings: galaxies: starburst — galaxies: halos — UV: galaxies — galaxies: individual (Haro11)

1. Introduction

Recent observations, headlined by the *WMAP* satellite, have ushered in a new era of "precision cosmology" (Bennett et al. 2003). Measurements of the age, geometry, density, and composition of the universe have led to a robust understanding of the evolution of its large scale structure (dominated by dark matter and dark energy). However, significant problems in ΛCDM simulations emerge when examining small scale structure and regions of high density where the complex range of baryonic physics becomes important (Klypin et al. 1999; Robertson et al. 2005; Sommer-Larsen et al. 1999). The frontier of cosmology is now in understanding the physical processes involved in the interactions between the intergalactic medium (IGM) and the gas, stars, and black holes that comprise galaxies.

At the forefront of this endeavor is understanding the role of feedback with which a galaxy mediates both its own evolution and that of the next generation of galaxies. Supernovae driven galactic scale winds appear to be an essential piece of galaxy evolution (Veilleux et al. 2005). In galaxies undergoing intense star formation, these winds drive gas, energy, and metals out of galaxies and possibly into the IGM (Heckman et al. 1998). Although common in the local universe, these winds were of particular importance in the past, due to the significantly higher overall star formation rate (SFR) in the early universe (Bunker et al. 2004).

Such winds at high redshift almost certainly had a profound impact on the energetics, ionization, and chemical composition of the IGM (Aguirre et al. 2005). For example, star-forming galaxies are thought to be an important source of ionizing photons in the early universe and could play a vital role in the reionization of the IGM. This effect should be enhanced by winds as they could clear paths through the neutral gas and dust surrounding the galaxy, allowing the ionizing photons to escape into the IGM (Dove et al. 2000). A reionized IGM strongly impacts galaxy formation as it suppresses gas cooling and subsequent infall into low mass halos (Barkana & Loeb 2006).

Multiwavelength observations are required to understand the complex multiphase nature of galactic winds (Strickland et al. 2004). The coronal gas ($T \sim 10^5$ to 10^6 K) and hot X-ray gas ($T \sim 10^6$ to 10^8 K) in galactic winds are particularly important. These phases are intimately connected to the mechanical/thermal energy that drives the outflows and to the metals the outflows carry. Far-ultraviolet (FUV) observations of the coronal gas provide important insights into the cooling and kinematics of the galactic winds (Heckman et al. 2001a; Hoopes, Heckman, Strickland, & Howk 2003). X-ray observations probe the slowly cooling hot gas that is most likely to escape the galaxy (Strickland & Stevens 2000).

The most widely studied population of high redshift star forming galaxies are the Lyman Break Galaxies (LBGs, Steidel et al. 1999). These galaxies can be efficiently detected for $2 \lesssim z \lesssim 6$ using the Lyman-break technique, which picks out spectral band dropouts caused by the 912 Å Lyman continuum discontinuity. They constitute a significant (and possibly dominant) fraction of the population of star forming galaxies during this important cosmic epoch (Peacock et al. 2000). The LBGs trace the most overdense regions of the universe, which are believed to be the progenitors of present day galaxy groups and clusters (Giavalisco 2002; Ouchi et al. 2004). They therefore play an important role in understanding the evolution of such clusters. Galactic winds appear to be a ubiquitous property of LBGs (Shapley et al. 2003). In particular, winds from LBGs could be the mechanism that heats and chemically enriches the Intra-cluster Medium (ICM, Helsdon & Ponman 2000; Tamura et al. 2004).

Unfortunately, our knowledge of the properties of the winds in LBGs is limited to what can be inferred from the interstellar UV absorption lines longward of Lyman α. Because of their great distance, X-ray detections are almost impossible using current X-ray observatories, although stacking techniques have been used to construct luminosity weighted average X-ray spectra (Nandra et al. 2002; Lehmer et al. 2005). A more fundamental problem is that the large redshifts of the LBGs mean that soft X-ray observations with *Chandra* or *XMM-Newton* are observing at rest-frame energies above a few keV. In local star-forming galaxies the emission in this band is dominated by the population of X-ray binaries, and the thermal emission from the galactic wind is negligible (Colbert et al. 2004). Likewise, observations of the coronal phase gas is very difficult in LBGs. The most accessible probe of such gas is the O VI $\lambda\lambda$1032,1038 doublet, which lies deep within the Lyman α forest in the spectra of LBGs.

It is clear that directly studying gas hotter than 10^5 K in high-redshift LBGs will continue to be very difficult or even impossible for the forseeable future. Therefore, an important step in understanding galactic winds in LBGs would be to identify the best local analogs to LBGs and to then investigate their winds using the full suite of observations that are possible at low redshift.

Recently Heckman et al. (2005) created a catalog of low redshift galaxies using *GALEX* (Martin et al. 2005) UV observations of galaxies with spectra taken by the Sloan Digital Sky Survey (SDSS, York et al. 2000). This catalog has now been significantly expanded based on additional *GALEX* data by Hoopes et al. (2006), who used this matched catalog to select a sample of extraordinarily rare local ($z < 0.3$) galaxies having the same UV luminosities, sizes, and surface brightnesses as typical LBGs. They then showed that these galaxies have the same star formation rates, galaxy masses, velocity dispersions, and chemical compositions as typical LBGs.

In the *GALEX* sample, VV 114 is the closest ($D_L \sim 86\,\mathrm{Mpc}$) known LBG analog. We have previously analyzed X-ray and FUV observations of VV 114 (Grimes et al. 2006). Diffuse thermal X-ray emission encompassing VV 114 was observed by *Chandra* and *XMM-Newton*. This hot ($kT \sim 0.59$ keV) gas has an enhanced α/Fe element ratio relative to solar abundances and follows the same relations as typical starbursts between its properties (luminosity, size, and temperature) and those of the starburst galaxy (SFR, dust temperature, galaxy mass). These results are consistent with the X-ray gas having been produced by shocks driven by a galactic superwind. The *FUSE* observations of VV 114 show strong, broad interstellar absorption lines with a pronounced blueshifted component (similar to what is seen in LBGs). This implies an outflow of material moving at $\sim 300 - 400\ \mathrm{km\,s^{-1}}$ relative to VV 114. The properties of the strong O VI absorption line are consistent with radiative cooling at the interface between the hot outrushing gas seen in X-rays and the cooler material seen in the other outflowing ions in the *FUSE* data. We also showed that the wind in VV 114 has *not* created a "tunnel" that would enable more than a small fraction (< few percent) of the ionizing photons from VV 114 to escape into the IGM.

The next closest LBG analog in the *GALEX* sample is Haro 11. Haro 11 is particularly interesting, as Bergvall et al. (2006) have claimed the detection of Lyman continuum radiation in the *FUSE* spectra. Bergvall et al. (2006) derived an escape fraction of $f_{esc} \sim 4 - 10\%$. This would make it the only known galaxy with Lyman continuum emission in the local universe and thus an ideal candidate to study this intriguing property of some high redshift LBGs (Shapley et al. 2006).

Haro 11, also known as ESO 350-IG38 ($\alpha_{2000} = 00^h36^m52\overset{s}{.}5$, $\delta_{2000} = -33°33'19''$), is a starbursting blue compact galaxy located ~88 Mpc. This distance was derived using $v_{sys} = 6180\,\mathrm{km\,s^{-1}}$ (Bergvall et al. 2006) and assuming $H_0 = 71\,\mathrm{km\,s^{-1}\,Mpc^{-1}}$. Haro 11's far-UV luminosity ($10^{10.3}\,L_\odot$) and effective surface brightness ($10^{9.4}\,L_\odot\,\mathrm{kpc^{-2}}$) are typical of LBGs (Heckman et al. 2005). An ACS far-UV continuum filter image of the center of Haro 11 is shown in Figure 1. Three separate starbursting nuclei are observed in the image. In deeper images, Haro 11 appears to have an irregular morphology suggestive of a merger. This is consistent with Hα velocity observations by Östlin et al. (2001) that show that Haro 11 is not dynamically relaxed. IRAS measured a high dust temperature for Haro 11 with $F_{60\mu m}/F_{100\mu m} \sim 1.3$ (Sanders et al. 2003), implying an unusually intense UV radiation field associated with a high star-formation rate per unit area. Bergvall et al. (2000)

suggest that the lack of cold gas could imply that Haro 11 is about to run out of the gas required to fuel the starburst. Lastly, it has a very low gas phase metallicity of ∼20% solar (Bergvall & Östlin 2002). This low metallicity is presumably related to the relatively low amount of dust extinction. Galaxy properties of Haro 11 and, for comparison, VV 114 are summarized in Table 1. While VV 114 has roughly four times the stellar mass and SFR, Haro 11 has a significantly higher UV surface brightness due to its smaller size.

2. The Data

2.1. *FUSE* Observations

FUSE was launched on June 25th, 1999. The *FUSE* instrument is composed of four separate mirrors each having its own Rowland circle spectrograph (Moos et al. 2000). Two mirrors are coated with Al+LiF and two with SiC. The LiF mirrors have better sensitivity in the 1000 Å $\lesssim \lambda \lesssim$ 1180 Å wavelength region, while the SiC are optimized for observations in the range between 900 Å to 1000 Å. During the period when our observations were taken, pointing stability was $\sim 0.5''$. The spectra are imaged onto two micro-channel plate (MCP) detectors each having an A and B side. Each side produces both a LiF and SiC spectrum, for a total of 8 spectra for every *FUSE* observation.

Six time-tag mode exposures of Haro 11 were obtained through the LWRS aperture ($30'' \times 30''$) on October 12, 2001. We have followed the standard data reduction methods for low S/N spectra. The raw exposure data was run through the CalFUSE 3.1.8 data pipeline to produce intermediate data (IDF) files and then the calibrated flux data. As thermally-induced rotations of the spectrograph gratings and mirror misalignment can cause small zero point shifts in the wavelength calibration, we then cross correlate the individual exposures. For Haro 11 the largest zero-point wavelength shift was very small at < 0.039 Å. These wavelength shifts were then retroactively applied to the individual IDF files. We combined the IDF files for the individual exposures to create one IDF file for each instrument channel. Extracting calibrated spectra from the longer, combined IDF files allows the CalFUSE pipeline to fit (and not just scale) the various backgrounds. In order to minimize the detector background, we have extracted our spectra using the smaller, point source detector regions instead of the usual extended source regions (Dixon et al. 2007). This is possible as a visual examination of the 2-D detector image shows no evidence of galaxy emission outside this smaller, point source extraction region. Although the exposure time is channel dependent, the final exposure lengths are similar for all channels. For reference, the LiF 1A channel had 14953 seconds of total exposure time with 11940 seconds falling during orbital night.

2.2. *Chandra* Observations

Haro 11 was observed by *Chandra*'s ACIS instrument on October 28, 2006. The target was observed in very faint mode with Haro 11 centered on the S3 aimpoint. We reprocessed the data with *ciao* 3.4.1 and followed the standard *Chandra* data reduction threads (Chandra Interactive Analysis of Observations CIAO). For spectra extraction we have used the *ciao* command *specextract* and a local background from a region surrounding the galaxy. Approximately 1851 counts are observed from Haro 11. As described previously in Grimes et al. (2005) we used a rescaled background image included in *CALDB* 3.3.0.1 to create smoothed background subtracted images. The rescaled background image was also used to create an X-ray radial profile of Haro 11 based on the 0.3 - 1.0 keV count data.

3. Discussion

3.1. Physical Properties of the Hot X-ray Gas

Figure 2 is a three color adaptively smoothed X-ray image of Haro 11 with 0.3-1.0 keV in red, 1.0-2.0 keV in green, and 2.0-8.0 keV in blue. Soft X-ray emission surrounds the galaxy and extends up to 6 kpc from the galaxy. The soft X-ray emission is also seen to have a similar morphology to the Hα emission in the adjacent image (Schmitt et al. 2006).

Knot B shows the strongest emission in the X-ray and Hα images but is the weakest knot in the UV. Kunth et al. (2003) observed that knot B is the reddest knot and exhibited Lyα absorption. In both the X-ray and UV imaging data there appears to be an absorption feature running across knot B from the NE to SW. In all three wavebands Knot C appears to be a single luminous star cluster while the UV image of knot A shows it to be an assembly of several resolved star clusters. This could explain knot C's relatively low X-ray surface brightness as compared to knots A and B.

A faint point source is visible SE of knot C in the X-ray image. It is coincident with knot D which was identified by Kunth et al. (2003) in their Lyα emission image of Haro 11 and therefore is unlikely to be a background AGN. We have extracted spectra of the point source using a local background region which includes the diffuse thermal emission surrounding the source. We detect a total of $\sim$ 22 counts from the source. We fit the spectra with a powerlaw and find $\Gamma \sim 1.6$ and a luminosity of $L_{0.3-8.0\,\mathrm{keV}} \sim 2.2 \times 10^{39}\,\mathrm{erg\,s^{-1}}$. The source's luminosity and location near a star forming region suggest a possible ultraluminous X-ray source (ULX) identification but are not conclusive.

The complete X-ray spectrum of Haro 11 is plotted in Figure 3. As we have done in previous work (Grimes et al. 2005, 2006), the spectrum was fit with an xspec model of wabs(vmekal + zwabs × powerlaw). We find a hot gas temperature of 0.68 keV (see Table 3 for the derived fit parameters). Using these fits we derive luminosities of $\mathrm{L}_{0.3-2.0\,\mathrm{keV,thermal}} \sim 7.2 \times 10^{40}\,\mathrm{erg\,s^{-1}}$ for the soft thermal component and $\mathrm{L}_{2.0-8.0\,\mathrm{keV,powerlaw}} \sim 1.0 \times 10^{41}\,\mathrm{erg\,s^{-1}}$ for the hard X-ray emission. We estimate a SFR from the powerlaw fit to the hard X-ray emission of $25\,\mathrm{M_{\odot}\,yr^{-1}}$ using the relation of Franceschini et al. (2003). This is in excellent agreement with the Hα, FIR, and radio continuum derived values given in Schmitt et al. (2006).

We also find an enhanced α/Fe ratio with a value of ~ 4 times the solar ratio. This is similar to the α/Fe ratios seen in in other starburst galaxies (e.g. Grimes et al. 2005). The enhanced α/Fe ratio is consistent with chemical enrichment of the hot gas by supernovae ejecta (Strickland et al. 2004). Due to the usual degeneracy of the abundance parameters, it is impossible to place strong constraints on the absolute α-element and Fe abundances. Figure 4 shows the 1-3 σ contours of χ^2 as a function of α-element and Fe abundances (relative to solar) from our fit to the X-ray spectra. The 20% oxygen gas phase metallicity derived in Bergvall & Östlin (2002) is significantly below our allowed range for the α-element abundances, again suggesting SN enrichment of the hot gas. Our best fit values for the absolute abundances of the hot gas are 1 and .25 solar for the α-elements and Fe respectively. If we assume an oxygen enrichment of ~ 6 (relative to solar) into the wind from supernovae (Limongi & Chieffi 2006) we can estimate β, the ratio of total mass added to the hot wind compared to that from stellar wind ejecta and SN (Strickland 2005). Our results suggest a mass loading in the hot wind fluid of $\beta \sim 7$.

It is also worth estimating the mass of material entrained in the hot X-ray gas. We can use the parameters for the fit to the total Chandra X-ray spectra of the diffuse gas in Haro 11 to derive estimates for the basic physical properties of the hot phase of the wind. The normalization for the VMEKAL component implies an emission integral (the volume integral of density squared) of 5.6×10^{63} cm^{-3}. For the geometrical volume of the emitting region we take a sphere whose radius encompasses 90% of the soft X-ray emission (∼2.7 kpc). This then implies a mean gas density of $n_e \sim 5 \times 10^{-2} f^{-1/2}$ cm^{-3} and a gas mass of $M \sim 1 \times 10^{8} f^{1/2}$ M$_{\odot}$ (where f is the volume filling factor of the X-ray emitting material). For kT = 0.68 keV the mean thermal pressure is $P = 1.1 \times 10^{-10} f^{-1/2}$ dyne cm^{-2} and the total thermal energy content of the hot gas is $E = 2.5 \times 10^{56} f^{1/2}$ erg.

Taking the characteristic timescale to be the above radius (2.7 kpc) divided by the sound speed in the hot gas ($\sim$ 450 km s^{-1}) yields an outflow age of 6 Myr. The implied outflow rates in the hot gas are then $\dot{M} \sim 18 f^{1/2}$ M$_{\odot}$ year^{-1} and $\dot{E} \sim 1.3 \times 10^{42} f^{1/2}$ erg s^{-1}. Since this neglects the kinetic energy in the wind material it probably underestimates the total energy transport rate by a factor of a few (Strickland & Stevens 2000). For volume filling factors similar to those estimated for other starburst winds ($f \sim 0.1$ to 1, Strickland et al. 2000), the implied mass outflow rate in Haro 11 is thus comparable to the total SFR of $\sim 25\ \mathrm{M}_\odot\,\mathrm{year}^{-1}$ (Schmitt et al. 2006). The rate of energy transport is similar to the total rate at which we estimate that mechanical energy would be supplied by supernovae and stellar winds in the starburst of $\sim 5 \times 10^{42}$ erg s^{-1}. This value was calculated using Starburst99 v5.1 assuming a Salpeter IMF from $1 - 100\,\mathrm{M}_\odot$ (Vázquez & Leitherer 2005). These outflow rates significantly exceed the rates for the cooler gas derived from the *FUSE* data below, but are typical of winds in powerful local starburst galaxies (e.g. Heckman 2003).

The Starburst99 calculations estimate a supernovae outflow rate of $\dot{\mathrm{M}}_{\mathrm{SN}} \sim 3.8\,\mathrm{M}_\odot\,\mathrm{year}^{-1}$. From the outflow rate of hot gas of $\dot{M} \sim 18 f^{1/2}\ \mathrm{M}_\odot\,\mathrm{year}^{-1}$, we find a mass loading of $\beta \sim 5\,f^{1/2}$. This value agrees well with our previous estimate of $\beta \sim 7$. It is also worth noting that the pressure and density derived for Haro 11 are almost identical to those in VV 114 with $P = 9.2 \times 10^{-11} f^{-1/2}$ dyne cm^{-2} and $n_e \sim 5 \times 10^{-2} f^{-1/2}$ cm^{-3} (Grimes et al. 2006).

3.2. *FUSE* Observations of the Wind

The *FUSE* data reveals a large number of absorption features, as shown in Figure 5. These absorption lines probe the stellar population, inter-stellar medium (ISM), and outflowing gas of Haro 11. We have fit absorption lines to most of the most promiment features using the IRAF (Tody & Fitzpatrick 1996) tool *specfit* (Kriss 1994). Each line was fit using a freely varying powerlaw for the continuum and a symmetric gaussian absorption line. When absorption lines are blended (e.g. O I λ989 and N III λ990), we have fit them simultaneously. For the majority of absorption lines we have used the LiF channels to make two independent measurements of the equivalent width, velocity, and full-width half-maximum (FWHM). For lines with only one measurement, the line either fell in the gap between LiF channels or was in the region (1125-1160Å) affected by partial light blocking by a wire grid (e.g. the worm) on the LiF 1B channel. We have ignored the SiC channels above 1000 Å due to their lower S/N. Tables 3 and 4 display the results of our fits to the data for the ISM lines and stellar photospheric lines respectively. Errors are 1σ and are calculated from the minimization error matrix which is re-scaled by the reduced χ^2 value (Kriss 1994).

We use the stellar photospheric lines as an independent measurement of the system velocity of Haro 11. Previous work by Bergvall et al. (2006) used Ca II absorption lines to derive a velocity of 6180 km s^{-1}. This compares favorably with our own measurements of 6163 - 6202 km s^{-1} from Si IV and P V stellar lines. Therefore we will use the value of 6180

$\mathrm{km\,s^{-1}}$ as the galaxy's systemic velocity.

The ISM lines in Table 3 suggest a centroid blueshift relative to the galaxy of ~ 100 $\mathrm{km\,s^{-1}}$. A closer examination of the line profiles shows that they are consistently asymmetric. This mild asymmetry in the line profile can be seen in Figure 6. There appears to be excess absorption on the blue side. The gaussian models are overestimating the FWHM in order to fit the absorption line profiles. In keeping with our previous work on VV 114, we have fit the strongest absorption lines with a second, blue absorption line. The results of our two-component fits are listed in Table 5.

We associate the stronger absorption feature in our fits with the host galaxy or a low velocity outflow. In general, the centroids of these lines are at $\sim 6100\,\mathrm{km\,s^{-1}}$. The central velocity is blueshifted $\sim 80\,\mathrm{km\,s^{-1}}$ relative to the host galaxy. The stronger absorption lines have FWHMs of $\sim 300\,\mathrm{km\,s^{-1}}$, suggesting that the lines do include the galaxy's ISM. The weaker absorption lines are generally at $\sim 5900\,\mathrm{km\,s^{-1}}$. We identify the second set of absorption lines with a high velocity outflow of material moving at $200 - 280\,\mathrm{km\,s^{-1}}$ away from the galaxy. Interestingly, a comparison of the equivalent widths of C II to C III and N II to N III show that the higher ionization lines are relatively stronger in the outflow as compared to the lower velocity absorption features. This could be a product of shocks between the outflow and the ambient material.

In Figure 6 it is clear that the coronal gas line O VIλ1032 has a different profile than the other ISM absorption lines. While the O VI centroid velocity of $6043 \pm 34\,\mathrm{km\,s^{-1}}$ is roughly consistent with those of the ISM absorption lines, there are significant discrepancies. First, a single absorption line fits O VI poorly, due to a weak blue wing extending several hundred $\mathrm{km\,s^{-1}}$ away from the galaxy. While this blue wing is relatively weak compared to the primary feature, it extends to much lower velocities (e.g. higher outflow velocities) than the blue wings we observe in some of the other absorption profiles. Secondly and more intriguingly, O VI emission appears to be present, forming part of a P-Cygni profile. An emission feature is observed at $6303 \pm 21\,\mathrm{km\,s^{-1}}$. This identification is supported by a corresponding emission feature for O VIλ1038 with a similar centroid at $6282 \pm 30\,\mathrm{km\,s^{-1}}$. They also have similar FWHMs of 185 ± 47 and 151 ± 55 $\mathrm{km\,s^{-1}}$ for O VIλ1032 and O VIλ1038 respectively. An absorption feature is not observed for O VIλ1038 but it is likely hidden in the broad C IIλ1036 absorption feature. In fact, the previously described two component absorption line profile for C II fits the red wing particularly poorly (Figure 6) and has a large FWHM, consistent with contamination by an O VIλ1038 absorption feature. The O VI$\lambda\lambda$1032, 1038 doublet is the only ion that we unambiguously identify in emission although there is a possible emission feature for C IIIλ977 at $6356\,\mathrm{km\,s^{-1}}$. The O VI P-Cygni profile has been previously identified by Bergvall et al. (2006).

Broad P-Cygni profiles are common for O VI in spectra of O stars (Pellerin et al. 2002). While a P-Cygni profile has not been observed in other starburst galaxies, the high UV surface brightness, low UV attenuation, and high SFR of Haro 11 could suggest that we are detecting an aggregate stellar profile. However, the observed O VI emission and absorption features are significantly narrower than those seen in stellar spectra. In particular, narrow O VI$\lambda\lambda$1032, 1038 emission is not observed in the stars in the sample of Pellerin et al. (2002). The narrow O VI feature is also inconsistent with the synthetic starburst spectra generated by Robert et al. (2003). We therefore explore the possibility that the O VI profile is not a stellar feature but is instead due to interstellar gas.

In previous analyses of starburst galaxies (e.g. Heckman et al. 2001a; Grimes et al. 2006) the O VI absorption has been the most blueshifted and broadest feature. The extreme outflow velocities of the O VI absorption suggests that in those galaxies, O VI is not produced directly by the cooler outflowing clouds responsible for the other absorption lines. Instead, Heckman et al. (2001a) attribute the production of O VI to the intermediate temperature regions created by the hydrodynamical interaction between hot outrushing gas and the cool fragments of the ruptured superbubble seen in Hα images. Such a situation is predicted to be created as an overpressured superbubble accelerates and then fragments as it expands out of the galaxy (Heckman et al. 2001a).

Heckman et al. (2002) derive a simple and general relationship between the O VI column density and absorption line width which holds whenever there is a radiatively cooling gas flow passing through the coronal temperature regime. They showed that this simple model accounted for the properties of O VI absorption line systems as diverse as clouds in the disk and halo of the Milky Way, high velocity clouds, the Magellanic Clouds, starburst outflows, and some of the clouds in the IGM (but see Tripp et al. 2007, in prep, for a more thorough test of the relation for IGM clouds). From our fit to the O VIλ1032 absorption feature we have derived a column density of $N_{OVI} = 4.2 \times 10^{14}\,cm^{-2}$. Haro 11 does fall within the scatter in the relationship, but we would expect a slightly higher O VI column density for the measured line width of $\sqrt{2}\sigma = b = 106\,km\,s^{-1}$. While the equivalent width and breadth of the O VI absorption are roughly consistent with O VI production in the interface between the outrushing gas and the cool shell fragments (Heckman et al. 2001a), the kinematics of O VI are inconclusive. Specifically, unlike our previous observations of VV 114 and NGC 1705 (Grimes et al. 2006; Heckman et al. 2001a), the primary O VI absorption feature is not blueshifted relative to the cooler, ISM lines.

O VI emission has previously been observed in only two spiral galaxies, NGC 4631 (Otte et al. 2003) and our own Milky Way (Dixon et al. 2006, and references therein). The O VI emission in the halo of NGC 4631 was attributed to cooling gas from a galactic chimney

(Otte et al. 2003). Similarly, for Haro 11 , we could attribute the O VI emission to radiatively cooling gas associated with the outflow. As O VI is the dominant coolant for gas at temperatures T $\sim 10^{5.5}$ K, O VI cooling could inhibit the ability of the outflowing gas to escape the galaxy. Therefore it is interesting to estimate the implied energy losses associated with the O VI emission.

The observed flux in O VI emission is $2.3 \pm 0.8 \times 10^{-14}\,\mathrm{erg\,s^{-1}\,cm^{-2}}$ and $1.4 \pm 0.5 \times 10^{-14}\,\mathrm{erg\,s^{-1}\,cm^{-2}}$ for the $\lambda1032$ and $\lambda1038$ lines respectively. While the O VI$\lambda1038$ flux could be an underestimate due to O I$\lambda1039$ absorption, these measured values are near the theoretical upper limit of $\mathrm{F_{OVI\lambda1032}/F_{OVI\lambda1038}} = 2$ found in an optically thin gas. We correct the fluxes for both galactic extinction and intrinisic dust attenuation. To correct for galactic extinction we use E(B-V)=0.011 (Schlegel et al. 1998) and assume the extinction law of Cardelli et al. (1989). For intrinsic attenuation we start with work by Seibert et al. (2005). They used *GALEX* and *IRAS* data to study the relationship between UV attenuation (1500 Å) and the IR excess. From Table 1 we find an IR excess for Haro 11 of $\log(\mathrm{L_{FIR}/L_{UV}}) = 0.53$. This IR excess correspond to $\mathrm{A_{1500\,\mathring{A}}} \sim 1.6$ mag (Seibert et al. 2005). We then extend this dust attenuation to 1035 Å following the work by Leitherer et al. (2002). They used Hopkins Ultraviolet Telescope (HUT) observations of star-forming galaxies to study dust attenuation at shorter wavelengths. They found a factor of 1.3 increase in the dust attenuation from 1500 to 1035 Å. We therefore calculate $\mathrm{A_{1035\,\mathring{A}}} \sim 2.1$ mag. Finally we estimate a total corrected O VI luminosity of $\sim 2.8 \times 10^{41}$ erg s^{-1}. O VI is responsible for $\sim 30\%$ of the cooling in coronal gas (Heckman et al. 2001a) so $\mathrm{L_{coronal}} \sim 9.3 \times 10^{41}$ erg s^{-1}. This luminosity is larger than Haro 11's thermal X-ray luminosity (7.2×10^{40} erg s^{-1}) and is comparable to both the energy outflow rate of the hot gas ($\dot{E} \sim 1.3 \times 10^{42} f^{1/2}$ erg s^{-1}) and the mechanical energy being input by supernovae ($\sim 5 \times 10^{42}$ erg s^{-1}). Therefore, if the O VI emission is produced by radiative cooling of the outflowing gas, it suggests that a significant percentage (20%) of the energy input from the supernovae could be radiated away by the coronal gas.

Several previous works have discussed the $\mathrm{L_{OVI}/L_{X-ray}}$ ratio. In their detection of O VI emission in NGC 4631, Otte et al. (2003) estimated $\mathrm{L_{OVI}/L_{X-ray}} \sim 0.11$. Although O VI emission was not observed in NGC 1705 and M82, lower limits of $\mathrm{L_{OVI}/L_{X-ray}} \lesssim 3$ (Heckman et al. 2002) and $\lesssim 0.4$ (Hoopes, Heckman, Strickland, & Howk 2003) were determined respectively. Our own result, $\mathrm{L_{OVI}/L_{X-ray}} \sim 3.9$ seems anomalously high in comparison to these previous results.

It is possible that the O VI emission line in Haro 11 is not tracing the rate at which coronal gas is radiatively cooling. Instead it may arise through resonant scattering of far-UV continuum photons from the starburst off O VI ions in the outflow. The redshift of the emission component is a natural consequence of such a picture (this is a classic P-Cygni profile). There is a shell of coronal gas flowing out from the starburst, and is traced by O VI ions. The front side of the flow is seen as blue-shifted absorption against the far-UV continuum of the starburst, while resonant scattering by O VI ions on the back side of the flow produces a red-shifted emission line. For a symmetric flow geometry, and in the absence of significant differential dust extinction of the OVI emission from the back side, this would predict that the equivalent widths of the blueshifted absorption and redshifted emission lines would be equal and opposite. This is roughly what is observed in Haro 11.

If this is the correct interpretation, the question is then why a redshifted emission component is not seen in the other ions (lower ionization states). This would have to mean that the O VI and cooler gas are not co-spatial: redshifted emission from the back side of an outflow is obscured by dust for the low ions, but not for O VI . This could be the case (for instance) if the size scale of the flow were significantly larger in OVI so that more of the back side lay beyond the region of significant dust extinction.

With the present data it is not possible to determine whether the O VI emission is produced by radiative cooling, or resonant scattering. If it's the latter, then the true contribution to radiative cooling by the coronal gas discussed above must be regarded as an upper limit. This reinforces the idea that radiative cooling is not significantly influencing the dynamics of the wind.

3.3. Escape of Ionizing Radiation?

Recent observations imply that the epoch of reionization occurred at a redshifts $6 < z < 20$ (Becker et al. 2001, Fan et al. 2002, Spergel et al. 2003). Several mechanisms have been proposed for reionization including UV photons from star formation or active galactic nuclei (AGN), X-ray photons from supernovae and mini-quasars (Oh 2001), and even sterile neutrino decay (Hansen & Haiman 2004). However X-ray background and cosmic microwave background (CMB) observations rule out significant contributions by X-ray photons and neutrino decays (Mapelli & Ferrara 2005; Dijkstra et al. 2004). UV photons from quasars likewise appear to be inadequate due to the rapidly falling space density of quasars at $z > 3$ (Fan et al. 2001). While recent work suggests that UV photons from stars could reionize the universe (Yan & Windhorst 2004), this inference is quite uncertain. First, the cosmic star formation at the relevant redshifts is still uncertain. Second, the fraction of ionizing photons that are able to escape to the IGM (f_{esc}) is even more uncertain.

The escape of ionizing continuum radiation from star forming galaxies was first observed by Steidel et al. (2001) in a sample of $z \sim 3.4$ LBGs. It has been suggested that the lower luminosity LBGs (e.g. $L < L_*$) could play an important role in reionization (Bouwens et al. 2006). Galactic winds appear to be a global property of LBGs (Shapley et al. 2003), and this may explain why a significant fraction of their ionizing radiation is able to escape.

More recent work by Shapley et al. (2006) focused on deep rest-frame UV spectroscopy of a sample of 14 LBGs. They detected significant Lyman continuum emission in only two of the galaxies. They found a sample-averaged relative Lyman continuum escape fraction of 14% but were unable to find a galaxy property that controlled the detection of the Lyman continuum. Their results suggest that even at high redshifts ($z \sim 3$) significant Lyman leakage is the exception.

Most recently Bergvall et al. (2006) published an analysis showing the detection of Lyman continuum emission in Haro 11. Haro 11's low neutral hydrogen mass limit of $\lesssim 10^8 M_\odot$ (Bergvall et al. 2006), high FUV surface brightness, irregular morphology, and low metallicity (Bergvall & Östlin 2002) all suggest that Haro 11 is an ideal local candidate for Lyman continuum emission. Haro 11's Lyman continuum leakage was in fact our prime motivation for obtaining *Chandra* data of the galaxy. As part of our analysis we have reanalyzed the *FUSE* data and have come to a different conclusion than the previous work by (Bergvall et al. 2006).

For the following discussion we focus primarily on the night only data. While we lose 4 ks (12 ks total night exposure) of observing time, the night background level is considerably lower and relatively well behaved. In Figure 7 we have plotted the extracted spectra for the SiC 2A and SiC 1B detectors. As discussed in section 2.1 we have used the standard extraction methods for low S/N spectra to produce these plots. The SiC 1B spectra show a negative flux, a common feature of low S/N LWRS spectra at these wavelengths. This is related to the difficulty in fitting the background models to the LWRS aperture region as it is near the bottom edge of the detector (see Figure 8). Unlike the SiC 1B spectra, the SiC 2A spectra have a small positive net flux.

The oversubtracted SiC 1B spectra suggests the relative importance of the background subtraction. Figure 8 shows images of the two micro-channel plates (MCPs) in the regions of interest. We have overlaid the point source extraction region and wavelength scales on the image. While galactic emission is clearly visible at wavelengths longward of Haro 11's Lyman break (~ 930.8 Å), there is no convincing visual evidence of Lyman continuum emission in these images. More importantly, possible emission features in SiC 2A are not replicated in the SiC 1B image. In order to examine the spectra more directly we have extracted the total counts in 1Å bins for a rectangular region approximating the source aperture. We have also extracted the same information from adjacent regions of the same size directly above and below the source aperture (Figure 9). These background profiles are similar to the source spectrum for wavelengths below the Lyman limit. If present, any Lyman continuum flux appears to be fainter than the variance present in the background regions.

In Figure 10 we show the regions flagged by the CalFUSE pipeline as possibly contaminated by geocoronal or scattered solar light. While these features are significantly weaker during orbital night, the region of interest between $920 - 930$Å is almost fully covered by these features. Determining the background in these regions is thus particularly difficult. Regions of background contamination were interpolated across when the *FUSE* scattered light background files were created (Dixon et al. 2007).

There are several components to the *FUSE* background. The intrinsic background of $\sim 0.5\,\mathrm{counts\,cm^{-2}\,s^{-1}}$ consists of beta decays from ^{40}K on the MCP glass and cosmic rays (Dixon et al. 2007). In addition, a contribution from geocoronal light varies from 20-300% of the intrinsic background during the orbit. The *FUSE* pipeline uses independent measurements of the dark count, night geocoronal scattered light, and day geocoronal scattered light to fit the background observed on **unilluminated** regions of the detector. An optimal extraction algorithm then extracts the source counts from the background (Horne 1986). Figure 11 shows the total counts and fitted background model for the SiC 2A night time data. The background clearly dominates the observed counts in the regions below the Lyman limit. While the fitted background is generally reasonable, it does over-subtract in some regions. This again highlights the difficulties in subtracting a temporally and spatially varying background from relatively low S/N data.

We have derived total fitted source and background fluxes for the SiC 2A night data in two wavelength ranges below the Lyman limit. From 920-925 Å we found a source flux of $1.9 \times 10^{-15}\,\mathrm{erg\,cm^{-2}\,s^{-1}\,\AA^{-1}}$ compared to a background flux of $8.7 \times 10^{-15}\,\mathrm{erg\,cm^{-2}\,s^{-1}\,\AA^{-1}}$. For comparison, we also examined the 925-930 Å region within which we would expect less airglow contamination (e.g. Figure 10). This region has a significantly lower source flux of $5.6 \times 10^{-16}\,\mathrm{erg\,cm^{-2}\,s^{-1}\,\AA^{-1}}$ with a comparable background of $6.1 \times 10^{-15}\,\mathrm{erg\,cm^{-2}\,s^{-1}\,\AA^{-1}}$. The source flux varies by a factor of ~ 3 between these two regions although we would not expect the Lyman continuum to vary strongly (Bergvall et al. 2006). A 20% error in the background subtraction would erase any source flux even in the 920-925 Å region.

As we have stated, the *FUSE* background varies significantly during an observation. Airglow and geocoronal scattered light both contribute to the background and vary depending on the pointing of the satellite relative to the earth. As the *FUSE* data is time-resolved, we can study the detector count rate as a function of wavelength and earth limb angle. In Figure 12 we have plotted the earth limb angle versus detector count rate for three wavelength regions. This plot includes both night and day data so that we could include the lowest earth limb angles. The Lyman continuum region is represented by the 920-930

Å points while the 930-940 Å and 940-940 Å regions contain some emission intrinsic to Haro 11. The Lyman continuum region has the lowest count rate for all earth limb angles. More importantly, as the earth limb angle increases, the count rate continues to fall even at the highest earth limb angles. We estimate an expected dark count rate from cosmic rays and ^{40}K of $\sim 0.05\,\mathrm{counts\,s^{-1}}$ which closely matches the count rate in the Lyman continuum region observed at the highest earth limb angles. This again suggests that the observed Lyman continuum emission is likely a systematic artifact of extracting low S/N spectra from a dominant and variable background.

For Figure 13 we have rescaled the SiC 1B background subtraction to match the observed SiC 2A spectra. In comparing the two spectra it is worthwhile to note that in the regions below 930 Å , possible spectral features are not replicated in both spectra. This also suggests that the detected emission is largely a combination of detector noise and systematic effects from the background subtraction.

A comparison to the results by Bergvall et al. (2006) of the SiC 2A data show a positive offset of the continuum level by $\sim 1\times10^{-14}\,\mathrm{erg\,cm^{-2}\,s^{-1}\,\text{Å}^{-1}}$. The continuum shapes however are similar. In the Bergvall et al. (2006) spectra it is worthwhile noting that none of the absorption lines are black. This includes two narrow Milky Way absorption lines C III λ977 and C II λ1036 which would be expected to be saturated at line center, independent of the properties of Haro 11. These lines are black in our spectra as seen in Figure 5.

As we are analyzing the same observational data, we have three possible reasons to explain the discrepancy between our results and those of Bergvall et al. (2006). First, we are using a newer version of the CalFUSE pipeline (3.1.8 versus 3.0) which includes several improvements in the background analysis. In particular v3.0 did not properly account for regions of the detector excluded because of airglow contamination and therefore frequently underestimated the total background. Secondly, we suspect that the extended source extraction region was used for the prior analysis by Bergvall et al. (2006). For Haro 11 the point source extraction region includes all of the source flux and has a higher S/N due to the smaller extraction region on the detector. Lastly, it is possible that the individual exposures were separately background subtracted. For low S/N spectra it is preferable to combine the exposures and allow the CalFUSE pipeline to fit a background model to the merged dataset. If the background subtraction is performed on the individual exposures of Haro 11 , the CalFUSE pipeline will simply scale the subtracted background by the exposure time. As the background is varying both spatially and temporally, this causes systematic offsets in the background subtraction. This explanation is likely as it would also explain the offset seen even in the relatively high S/N LiF 1A spectra of Bergvall et al. (2006).

Although we find no convincing evidence for Lyman continuum emission it is useful to derive an upper limit. Following Bergvall et al. (2006) we use the 920-925 Å flux and correct for galactic extinction. We derive $f_{900} \lesssim 2.3 \pm 0.7 \times 10^{-15}\,\mathrm{erg\,cm^{-2}\,s^{-1}\,\AA^{-1}}$ as compared to the previous result of $f_{900} = 1.1 \pm 0.1 \times 10^{-14}\,\mathrm{erg\,cm^{-2}\,s^{-1}\,\AA^{-1}}$ (Bergvall et al. 2006). Our 1σ errors are purely statistical and do not include the dominant systematic errors. Using our derived value of f_{900} and the formulism for deriving $f_{\rm esc}$ derived by Bergvall et al. (2006), we find $f_{\rm esc} \lesssim 2\%$.

3.4. X-ray Properties of LBG Analogues

In Grimes et al. (2005) we analyzed *Chandra* observations of the diffuse emission in 23 star-forming galaxies. We showed that the properties of the hot gas (e.g. temperature, metal enrichment, and luminosity) were remarkably consistent throughout the sample. These findings suggested that the same physical mechanism was producing the diffuse X-ray emission throughout the sample. We found that shocks, driven by a galactic "superwind" powered by the kinetic energy collectively supplied by stellar winds and supernovae in the starburst, were the likely explanation for this correspondence. As we have now obtained deep *Chandra* observations of two LBG analogues, it is worth examining how they fit within this framework. While it is 'dangerous' to make general conclusions based on such a small sample size, it is worth discussing as few LBG analogues are currently observable in the X-ray without unreasonable exposure times.

Haro 11 and VV 114 were selected due to their high UV luminosities and compact size. This suggests a high SFR compared to galaxies of similar mass (see Heckman et al. (2005)). Given the selection criteria, we find that the properties of the hot gas follow accordingly. The left panel of Figure 14 is a plot of $L_{\rm FIR} + L_{\rm UV}$ (a proxy for SFR) versus the thermal 0.3-2.0 keV X-ray luminosity. This plot is originally taken from Grimes et al. (2005) and includes dwarf starbursts, starbursts, and ULIRGs. There is a clear correlation (possibly non linear) between the thermal X-ray emission and the SFR. Haro 11 and VV 114 fall between the starbursts and ULIRGs as expected for LBG analogues. In the right-hand panel we have divided the thermal X-ray and FIR+UV luminosities by the K-band luminosity (a proxy for stellar mass). This shows a fundamental connection between the level of star formation and the luminosity of the thermal X-ray gas. Unsurprisingly, both VV 114 and Haro 11 have high SFRs and soft X-ray luminosities given their stellar mass.

In Grimes et al. (2005) we showed that both the K-band and FIR luminosities scaled with the radial extent of the soft X-ray emission. In Figure 15 we have plotted the 0.3-1.0 keV 90% flux enclosed radius versus the FIR and K-band luminosities. Due to the high SFRs and compact sizes, both Haro 11 and VV 114 fall below the FIR relation for other starbursts.

Previously, the K-band relation had been only marginally preferred to the FIR-band relation based on Kendall's rank-order correlation coefficient. The chances of a spurious correlation were 2.7×10^{-5} versus 3.4×10^{-5} for K-band and FIR respectively. With the two new data points the chance of a spurious relation is unchanged for the FIR data. However the K-Band relation improved with a chance of a spurious correlation of 4.4×10^{-6}. This suggests that the host galaxy has a strong effect on the spatial extent of the X-ray emission, although the starburst drives the energetics and composition of the hot gas.

Figure 16 has a plot of the X-ray temperature versus the dust temperature (as traced by the IRAS F60μm/F100μm ratio). While most of the galaxies show a rough correlation Haro 11 with F60μm/F100μm=1.29 (Soifer, Boehmer, Neugebauer, & Sanders 1989) is one of the outliers. Physically, as the FIR emission is reprocessed UV light, F60μm/F100μm corresponds to the luminosity-weighted mean dust temperature which is set by the mean FUV intensity in the starburst ($\propto$ SFR per unit area). Knot B appears to be a compact region of intense star formation as it is the brightest feature in Hα , X-ray, Spitzer IRAC and MIPS, and 3.6 cm radio data (Schmitt et al. 2006). Knot B is probably dominating the observed IRAS F60μm/F100μm ratio and driving the anomalously high SFR per area.

4. Conclusions

Star formation driven feedback is an essential ingredient to understanding galaxy evolution and the IGM. Observations of local starbursts have shown that galactic winds, driven by the kinetic energy from supernovae and stellar winds, are the strongest manifestation of star formation driven feedback. These outflows are complex multi-phase phenomena whose physical, chemical, and dynamical properties can only be understood through complementary observations at many wavebands and detailed modeling (Veilleux et al. 2005). Observations of the coronal (10^5 to 10^6 K) and hot (10^6 to 10^7 K) gas are particularly important, as they provide essential information about the importance of radiative cooling of the outflow and about the dynamics and energy content of the wind. The coronal gas is best traced through the O VI doublet in the far-UV and the hot gas is best observed via its soft X-ray emission.

The strong overall cosmic evolution in the global SFR (e.g. Bunker et al. 2004) implies that the bulk of the feedback from galactic winds occurred at early times ($z > 1$). Indeed, the direct signature of galactic winds – the presence of broad, blueshifted interstellar absorption lines in the rest-frame UV – is generically present in the LBGs (Shapley et al. 2003). These are the best-studied population of high-redshift star forming galaxies (Steidel et al. 1999). However, such data provide only a narrow range of information about galactic winds. Unfortunately, direct observations of the hotter gas in the rest-frame soft X-ray and FUV regions for high redshift galaxies are extremely difficult or even impossible to obtain, which hinders progress in understanding this complex phenomenon. Finding and studying analogs to LBGs is therefore very important as a proxy for studying the outflow phenomenon.

In this paper we have described FUV and soft X-ray observations of Haro 11, the second Lyman break analogue observed by *Chandra*. Our *FUSE* observations in the FUV show strong and broad interstellar absorption lines. The lines with the highest S/N show two kinematic components. One is centered near the galaxy's systemic velocity and apparently includes the ISM. The second component is strongly blueshifted, suggesting an outflowing wind with a velocity of $\sim 200 - 280\,\mathrm{km\,s^{-1}}$. This is consistent with what is seen at slightly longer rest wavelengths in high redshift LBGs and further establishes the similarity of Haro 11 to the LBGs. The O VI feature has a P-Cygni profile that is not seen in other starbursting galaxies. While we are not able to clearly determine whether the source of the O VI emission is radiatively cooling or resonance scattering, we estimate that $\lesssim 20\%$ of the available energy from supernovae could be lost to radiative cooling. This suggests that O VI radiative losses do not significantly inhibit the growth of the outflow in Haro 11.

The wind in Haro 11 might in principle be able to carve a channel in the ISM through which ionizing photons could escape from the starburst to the IGM. However, our re-analysis of the *FUSE* observations shows that there is no convincing evidence of Lyman continuum leakage. This result is in contradiction to a previous report by Bergvall et al. (2006).

Observations with *Chandra* of the hot diffuse gas in Haro 11 are consistent with those seen in a local sample of star forming galaxies with galactic outflows. As expected based on its far-IR luminosity and implied SFR, Haro 11 has X-ray properties intermediate between those of ULIRGs and those of more typical present-day starbursts. It has X-ray properties very similar to that of VV 114, the only other LBG analogue mapped with *Chandra*. This suggests that diffuse thermal X-ray emission should be a common feature of LBGs created in the shocks between the outflowing wind material and surrounding medium (Marcolini et al. 2005).

J. G. thanks Henrique Schmitt for providing the Hα image of Haro 11 and Claus Leitherer for helpful discussions on the UV properties of stellar winds. Funding for this research was provided by NASA through Chandra Proposal 8610240.

REFERENCES

Aguirre, A., Schaye, J., Hernquist, L., Kay, S., Springel, V., & Theuns, T. 2005, ApJ, 620, L13

Anders, E., & Grevesse, N. 1989, Geochim. Cosmochim. Acta, 53, 197

Asplund, M., Grevesse, N., & Sauval, A. J. 2005, ASP Conf. Ser. 336: Cosmic Abundances as Records of Stellar Evolution and Nucleosynthesis, 336, 25

Barkana, R., & Loeb, A. 2006, MNRAS, 371, 395

Bennett, C. L., et al. 2003, ApJS, 148, 1

Bergvall, N., Masegosa, J., Östlin, G., & Cernicharo, J. 2000, A&A, 359, 41

Bergvall, N., Östlin, G. 2002, A&A, 390, 891

Bergvall, N., Zackrisson, E., Andersson, B.-G., Arnberg, D., Masegoas, J., & Ostlin, G. 2006, A&A, 448, 513

Bunker, A. J., Stanway, E. R., Ellis, R. S., & McMahon, R. G. 2004, MNRAS, 355, 374

Cardelli, J. A., Clayton, G. C., & Mathis, J. S. 1989, ApJ, 345, 245

Carpenter, J. M. 2001, AJ, 121, 2851

Chandra Interactive Analysis of Observations (CIAO), http://cxc.harvard.edu/ciao/

Charlot, S., & Longhetti, M. 2001, MNRAS, 323, 887

Colbert, E. J. M., Heckman, T. M., Ptak, A. F., Strickland, D. K., & Weaver, K. A. 2004, ApJ, 602, 231

Dixon, W. V. D., Sankrit, R., & Otte, B. 2006, ApJ, 647, 328

Dixon, W. V., et al. 2007, PASP, 119, 0

Dove, J. B., Shull, J. M., & Ferrara, A. 2000, ApJ, 531, 846

Franceschini, A., et al. 2003, MNRAS, 343, 1181

Giavalisco, M. 2002, ARA&A, 40, 579

Grimes, J. P., Heckman, T., Hoopes, C., Strickland, D., Aloisi, A., Meurer, G., & Ptak, A. 2006, ApJ, 648, 310

Grimes, J. P., Heckman, T., Strickland, D., & Ptak, A. 2005, ApJ, 628, 187

Heckman, T. M., Robert, C., Leitherer, C., Garnett, D. R., & van der Rydt, F. 1998, ApJ, 503, 646

Heckman, T. M., Sembach, K. R., Meurer, G. R., Strickland, D. K., Martin, C. L., Calzetti, D., & Leitherer, C. 2001, ApJ, 554, 1021

Heckman, T. M., Norman, C. A., Strickland, D. K., & Sembach, K. R. 2002, ApJ, 577, 691

Heckman, T. M. 2003, Revista Mexicana de Astronomia y Astrofisica Conference Series, 17, 47

Heckman, T. M., et al. 2005, ApJ, 619, L35

Helsdon, S. F., & Ponman, T. J. 2000, MNRAS, 315, 356

Hoopes, C. G., Heckman, T. M., Strickland, D. K., & Howk, J. C. 2003, ApJ, 596, L175

Horne, K. 1986, PASP, 98, 609

Jarrett, T. H., Chester, T., Cutri, R., Schneider, S. E., & Huchra, J. P. 2003, AJ, 125, 525

Kim, D.-C., Sanders, D. B., Veilleux, S., Mazzarella, J. M., & Soifer, B. T. 1995, ApJS, 98, 129

Klypin, A., Kravtsov, A. V., Valenzuela, O., & Prada, F. 1999, ApJ, 522, 82

Kunth, D., Leitherer, C., Mas-Hesse, J. M., Östlin, G., & Petrosian, A. 2003, ApJ, 597, 263

Kriss, G. 1994, ASP Conf. Ser. 61: Astronomical Data Analysis Software and Systems III, 61, 437

Lehmer, B. D., et al. 2005, AJ, 129, 1

Leitherer, C., Li, I.-H., Calzetti, D., & Heckman, T. M. 2002, ApJS, 140, 303

Limongi, M., & Chieffi, A. 2006, ArXiv Astrophysics e-prints, arXiv:astro-ph/0611140

Marcolini, A., Strickland, D. K., D'Ercole, A., Heckman, T. M., & Hoopes, C. G. 2005, MNRAS, 362, 626

Martin, D. C., et al. 2005, ApJ, 619, L1

Moos, H. W., et al. 2000, ApJ, 538, L1

Nandra, K., Mushotzky, R. F., Arnaud, K., Steidel, C. C., Adelberger, K. L., Gardner, J. P., Teplitz, H. I., & Windhorst, R. A. 2002, ApJ, 576, 625

Östlin, G., Amram, P., Bergvall, N., Masegosa, J., Boulesteix, J., & Márquez, I. 2001, A&A, 374, 800

Otte, B., Murphy, E. M., Howk, J. C., Wang, Q. D., Oegerle, W. R., & Sembach, K. R. 2003, ApJ, 591, 821

Ouchi, M., et al. 2004, ApJ, 611, 685

Peacock, J. A., et al. 2000, MNRAS, 318, 535

Pellerin, A., et al. 2002, ApJS, 143, 159

Robert, C., Pellerin, A., Aloisi, A., Leitherer, C., Hoopes, C., & Heckman, T. M. 2003, ApJS, 144, 21

Robertson, B., Bullock, J. S., Font, A. S., Johnston, K. V., & Hernquist, L. 2005, ApJ, 632, 872

Sanders, D. B. & Mirabel, I. F. 1996, ARA&A, 34, 749

Sanders, D. B., Mazzarella, J. M., Kim, D.-C., Surace, J. A., & Soifer, B. T. 2003, AJ, 126, 1607

Schlegel, D. J., Finkbeiner, D. P., & Davis, M. 1998, ApJ, 500, 525

Schmitt, H. R., Calzetti, D., Armus, L., Giavalisco, M., Heckman, T. M., Kennicutt, R. C., Jr., Leitherer, C., & Meurer, G. R. 2006, ApJS, 164, 52

Seibert, M., et al. 2005, ApJ, 619, L55

Shapley, A. E., Steidel, C. C., Pettini, M., Adelberger, K. L., & Erb, D. K. 2006, ApJ, 651, 688

Shapley, A. E., Steidel, C. C., Pettini, M., & Adelberger, K. L. 2003, ApJ, 588, 65

Soifer, B. T., Boehmer, L., Neugebauer, G., & Sanders, D. B. 1989, AJ, 98, 766

Sommer-Larsen, J., Gelato, S., & Vedel, H. 1999, ApJ, 519, 501

Steidel, C. C., Adelberger, K. L., Giavalisco, M., Dickinson, M., & Pettini, M. 1999, ApJ, 519, 1

Strickland, D. K., Heckman, T. M., Weaver, K. A., & Dahlem, M. 2000, AJ, 120, 2965

Strickland, D. K., & Stevens, I. R. 2000, MNRAS, 314, 511

Strickland, D. K., Heckman, T. M., Colbert, E. J. M., Hoopes, C. G., & Weaver, K. A. 2004, ApJ, 606, 829

Strickland, D. K. 2005, Extra-Planar Gas, 331, 345

Tamura, T., Kaastra, J. S., den Herder, J. W. A., Bleeker, J. A. M., & Peterson, J. R. 2004, A&A, 420, 135

Tody, D., & Fitzpatrick, M. 1996, Astronomical Data Analysis Software and Systems V, 101, 322

Vader, J. P., Frogel, J. A., Terndrup, D. M., & Heisler, C. A. 1993, AJ, 106, 1743

Vázquez, G. A., & Leitherer, C. 2005, ApJ, 621, 695

Veilleux, S., Cecil, G., & Bland-Hawthorn, J. 2005, ARA&A, 43, 769

York, D. G., et al. 2000, AJ, 120, 1579

This preprint was prepared with the AAS LaTeX macros v5.2.

Table 1. Comparison of Haro 11 versus VV 114

	Position J2000		Distance Mpc	v_{sys} $km\,s^{-1}$	Scale kpc arcsec^{-1}	Z	L_{FIR} [a] $L_\odot$	L_K [a] $L_\odot$	L_{FUV} [b] $L_\odot$	I_{FUV} [c] $L_\odot$ kpc^{-2}
Haro 11	+00 36 52.5	-33 33 19	88	6180	0.41	7.9[c]	6.7×10^{10}	4.5×10^{9}	2.0×10^{10}	2.8×10^{9} [d]
VV 114	+01 07 47.1	-17 30 24	86	5970[e]	0.40	8.6-8.7[f]	2.6×10^{11}	2.0×10^{10}	2.5×10^{10}	7.8×10^{8} [g]

[a] IRAS (Soifer, Boehmer, Neugebauer, & Sanders 1989) and 2MASS (Jarrett et al. 2003) results are transformed using methods of Sanders & Mirabel (1996) and Carpenter (2001) respectively.

[b] Derived from the *FUSE* continuum flux at 1150 Å

[c] Gas phase metallicity as log(O/H)+12 from Bergvall & Östlin (2002).

[d] ACS observation

[e] Grimes et al. (2006)

[f] Gas phase metallicity as log(O/H)+12 from Kim et al. (1995) using the transformations of Charlot & Longhetti (2001).

[g] GALEX observation

Table 2. Haro 11 X-Ray Spectral Fit[a]

$\mathrm{N_H}$[b] 10^{22} cm^{-2}	kT keV	K[c]	α/Fe	N_H 10^{22} cm^{-2}	PL Norm[d]	Γ	χ^2/DOF	$\mathrm{L_{0.3-2.0\,keV,thermal}}$ erg s^{-1}	$\mathrm{L_{2.0-8.0\,keV,powerlaw}}$ erg s^{-1}
1.9×10^{-2}	$0.68^{+0.05}_{-0.03}$	$6.0^{+1.4}_{-4.1} \times 10^{-5}$	$4.0^{+1.1}_{-1.2}$	$0.5^{+0.3}_{-0.5}$	$3.3^{+1.3}_{-1.6} \times 10^{-5}$	$1.7^{+0.3}_{-0.3}$	61/65	7.2×10^{40}	1.0×10^{41}

[a] Values derived from an xspec model of wabs (vmekal + zwabs (powerlaw)) using the default abundance settings (Anders & Grevesse 1989).

[b] Galactic $\mathrm{N_H}$ value fixed to COLDEN result

[c] Plasma model normalization in units of $\frac{10^{-14}}{4\pi[D_A(1+z)]^2}\int n_e n_H dV$, where D_A is the angular distance, and n_H and n_e are the hydrogen and electron number densities respectively.

[d] photons keV^{-1} cm^{-2} s^{-1} at 1 keV

Table 3. ISM Absorption Line Fit Data

Ion	λ_0 Å	$log(\lambda f N/N_H)$	Instrument	W_λ Å	v_c km s^{-1}	FWHM km s^{-1}
Ly β[b]	1025.722	1.91	LiF 1A	2.3 ± 0.1	6055 ± 9	557 ± 31
			LiF 2B	2.3 ± 0.1	6051 ± 9	529 ± 54
C III[b]	977.02	-0.61	LiF 1A	0.9 ± 0.2	6081[a]	169 ± 18
			LiF 2B	0.7 ± 1.4	6133[a]	87 ± 14
O VI	1031.926	-1.13	LiF 1A	0.4 ± 0.1	6042 ± 16	193 ± 35
			LiF 2B	0.4 ± 0.1	6051 ± 15	159 ± 34
C II	1036.337	-1.37	LiF 1A	1.4 ± 0.1	6061 ± 6	402 ± 19
			LiF 2B	1.2 ± 0.1	6075 ± 8	341 ± 30
O I	988.733	-1.56	LiF 1A	0.7 ± 0.1	6092 ± 13	275 ± 15
			LiF 2B	0.7 ± 0.1	6079 ± 23	304 ± 26
N II	1083.99	-2.00	LiF 1B	0.9 ± 0.1	6081 ± 10	352 ± 28
			LiF 2A	1.0 ± 0.1	6085 ± 11	381 ± 33
N III	989.799	-2.03	LiF 1A	1.0 ± 0.1	6076 ± 6	275 ± 137
			LiF 2B	1.1 ± 0.1	6073 ± 10	304 ± 152
N I	1134.415	-2.09	LiF 2A	0.2 ± 0.1	6074[a]	103 ± 36
O I	1039.23	-2.29	LiF 1A	0.3 ± 0.1	6110 ± 5	207 ± 47
			LiF 2B	0.3 ± 0.1	6135 ± 13	192 ± 46
Fe II	1096.877	-2.96	LiF 1B	0.3 ± 0.1	6101 ± 15	197 ± 72
			LiF 2A	0.2 ± 0.1	6127 ± 17	143 ± 40
Si II	1020.699	-2.989	LiF 1A	0.1 ± 0.1	6071 ± 37	87 ± 83
			LiF 2B	0.2 ± 0.1	6071 ± 12	100 ± 23
Fe II	1121.975	-3.15	LiF 2A	0.3 ± 0.2	6088 ± 68	203 ± 193
S III	1012.502	-3.24	LiF 1A	0.5 ± 0.2	6083 ± 6	225 ± 108
			LiF 2B	0.6 ± 0.2	6078 ± 13	290 ± 75
Fe II	1125.448	-3.41	LiF 2A	0.2 ± 0.1	6062 ± 17	195 ± 37
Ar I	1066.66	-3.59	LiF 2A	0.5 ± 0.2	6136 ± 27	332 ± 82

[a] Errors are undetermined for this value.

[b] Ly β and C III are saturated at line center.

Table 4. Stellar Photospheric Absorption Line Fit Data

Ion	λ_0 Å	Instrument	W_λ Å	v_c km s^{-1}	FWHM km s^{-1}
Si IV	1122.487	LiF 2A	0.6 ± 0.1	6163 ± 17	222 ± 29
Si IV	1128.201	LiF 2A	0.3^{a}	6202^{a}	327^{a}
P V	1117.977	LiF 2A	0.3 ± 0.1	6165 ± 24	320 ± 63^{a}
P V	1128.0	LiF 2A	0.1^{a}	6202^{b}	327^{b}

[a] Errors are undetermined for this value.

[b] Values of the velocity shift and FWHM of P V λ1128 are tied to the corresponding parameters in Si IV λ1128

Table 5. Two Component Absorption Line Fits

Ion	λ_0 Å	$log(\lambda f N/N_H)$	Instrument	Galaxy			Outflow		
				W_λ Å	v_c km s^{-1}	FWHM km s^{-1}	W_λ Å	v_c km s^{-1}	FWHM km s^{-1}
Ly β[a]	1025.722	1.91	LiF 1A	2.22 ± 0.07	6060 ± 7	519 ± 19	0.25 ± 0.09	5781 ± 18	124 ± 40
			LiF 2B	1.91 ± 0.15	6103 ± 20	467 ± 31	0.56 ± 0.16	5827 ± 21	184 ± 47
C III[a]	977.02	-0.61	LiF 1A	0.85 ± 0.18	6084 ± 6	146 ± 13	0.44 ± 0.18	5840 ± 7	60[b]
			LiF 2B	0.69[b]	6133 ± 4	83 ± 9	0.36[b]	5894 ± 6	53 ± 25
C II	1036.337	-1.374	LiF 1A	1.22 ± 0.09	6076 ± 8	356 ± 28	0.11 ± 0.05	5855 ± 27	100[b]
			LiF 2B	1.18 ± 0.10	6084 ± 12	325 ± 26	0.10 ± 0.17	5866 ± 70	104 ± 164
N II	1083.99	-2.002	LiF 1B	0.79 ± 0.14	6104 ± 12	310 ± 50	0.13 ± 0.05	5935 ± 11	88 ± 26
			LiF 2A	1.05 ± 0.20	6114 ± 20	392 ± 63	0.07 ± 0.20	5921 ± 39	123[b]
N III[c]	989.799	-2.03	LiF 1B	0.81 ± 0.04	6099 ± 11	217 ± 27	0.35 ± 0.13	5957 ± 22	150 ± 40
			LiF 2A	0.78 ± 0.22	6120 ± 31	268 ± 41	0.41 ± 0.17	6022 ± 17	128 ± 38

[a] The galaxy and/or outflow component of this line is saturated.

[b] Unable to determine errors on this value.

[c] N III λ990 is blended with O I λ989. They are fit simultaneously with the tied values of the fwhm and relative velocity.

Table 6. Mass and Energy Outflow Rates

Ion	N_{Ion}[a] 10^{14} cm^{-2}	Abundance[b] $\log(N_{Elem}/N_H) + 12$	N_H 10^{18} cm^{-2}	$\frac{\Omega}{4\pi}\dot{M}$[c] $M_\odot$/yr	$\frac{\Omega}{4\pi}\dot{E}$[c] 10^{40} erg/s
N II	1.4	7.78	2.3	0.1	0.2
N III	5.7	7.78	9.5	0.3	0.7
C II	3.6	8.39	1.5	0.1	0.1
Total Cool Gas[d]			>11.8	>0.4	>0.9
Total Hot Gas[e]				$18f^{1/2}$	$130f^{1/2}$

[a] Based on outflow equivalent width and FWHM from Table 5.

[b] Asplund et al. (2005)

[c] Estimated mass and kinetic energy outflow rates (see text).

[d] From *FUSE* data using N II and N III.

[e] From X-ray data. Note that f is the volume filling factor of the hot gas.

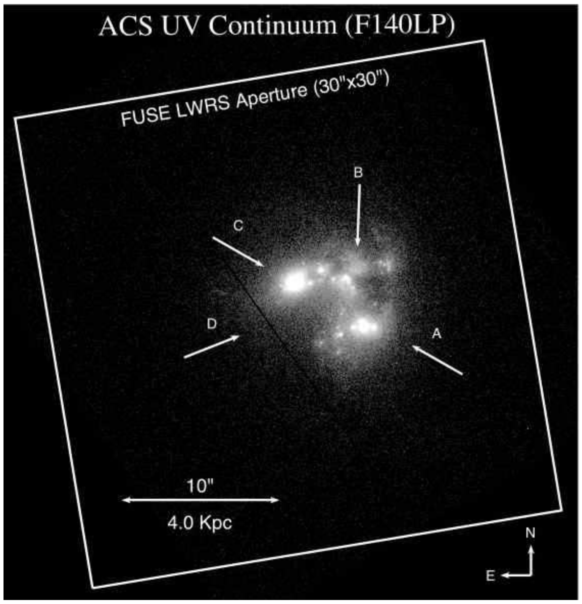

Fig. 1.— *FUSE* LWRS aperture overlaid on an HST/ACS FUV (F140LP) continuum image of Haro 11. We have also labeled the three knots (A-C) as in Vader et al. (1993). A fourth knot, identified by Kunth et al. (2003) is labeled D, although it is not visible in this image.

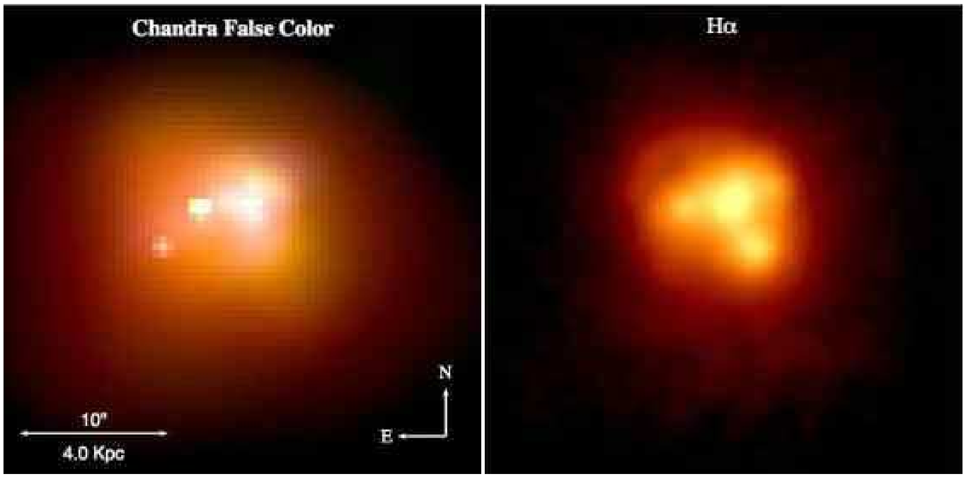

Fig. 2.— *Chandra* false color (red 0.3-1.0 keV, green 1.0-2.0 keV, blue 2.0-8.0 keV) and Hα (Schmitt et al. 2006) images of Haro 11. The two images have a similar morphology. Knot B, likely the galaxy nucleus, is the dominant feature in both the X-ray and Hα. The *Chandra* image suggests a narrow band/disk of absorption running NE to SW through knot B. This absorption feature also appears in the ACS FUV image (Figure 1). Knot D (SE of B), observed by Kunth et al. (2003) in Lyα emission, is only seen in the *Chandra* image.

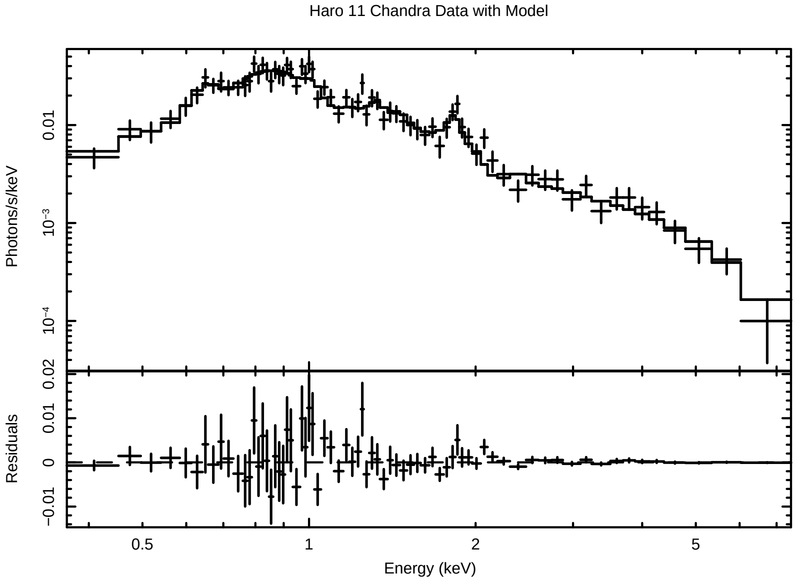

Fig. 3.— *Chandra* spectrum and model of Haro 11. The model fit parameters can be found in Table 2.

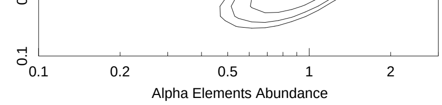

Fig. 4.— Contour plot (1-3 σ) of the variance in χ^2 as a function of α-element and Fe abundances (relative to solar) from the *xspec* fit to the X-ray spectrum. Although it is impossible to determine the absolute abundances, the α-element abundance (dominated by oxygen) in the hot gas is significantly enhanced relative to the 20% oxygen gas phase metallicity derived in Bergvall & Östlin (2002).

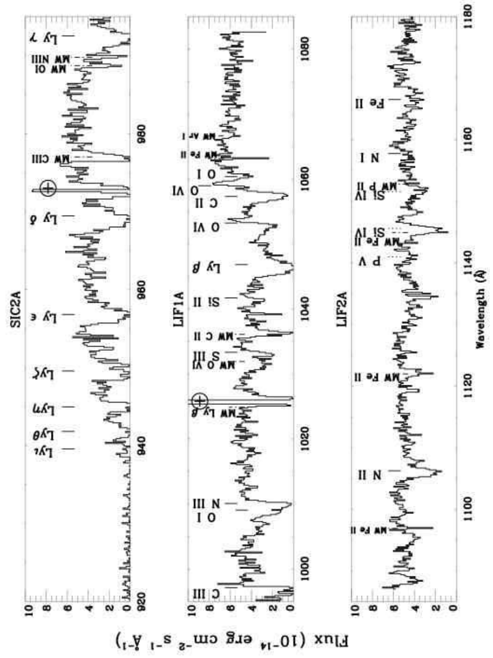

Fig. 5.— SiC 2A, LiF 1A, and LiF 2A spectra of Haro 11 covering the majority of the *FUSE* spectral range. Prominent Haro 11 absorption lines, milky way lines, and airglow features (earth symbol) have been identified.

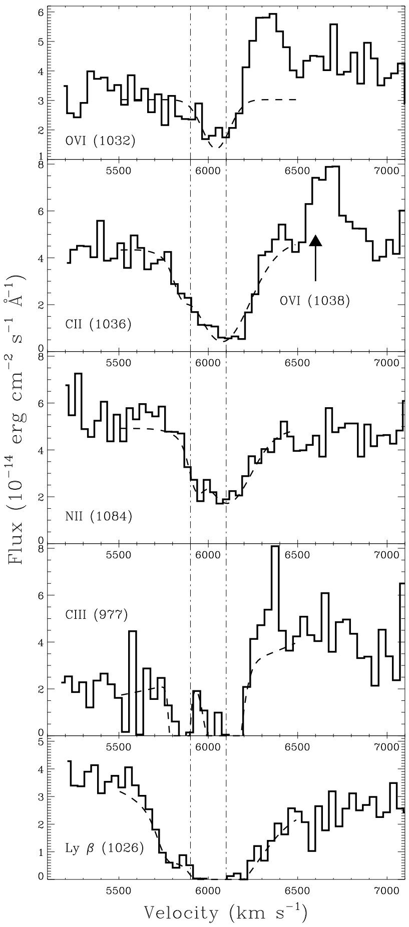

Fig. 6.— Expanded plots of five strong absorption features in the *FUSE* spectra of Haro 11. All of the absorption lines except O VI show signs of one strong, broad absorption line at ~ 6100 km s^{-1} and another weaker absorption line at ~ 5900 km s^{-1}. Both are significantly blueshifted relative to the galaxy systemic velocity of 6180 km s^{-1}. We have overlaid two component absorption line fits for the N II, C III, C II, and Ly β lines and vertical lines at 5900 and 6100 km s^{-1} for visual comparison. The absorption feature at 5900 km s^{-1} is clearly visible in the spectra although there is some variability in the centroid velocity. The O VI λ1032 line has a P-Cygni profile as it has absorption on the blue wing and emission on the red side. For O VI we have plotted a single absorption line although it does not well represent its non gaussian profile. O VI λ1038 emission (and possibly absorption) is observed in the C II λ1036 plot.

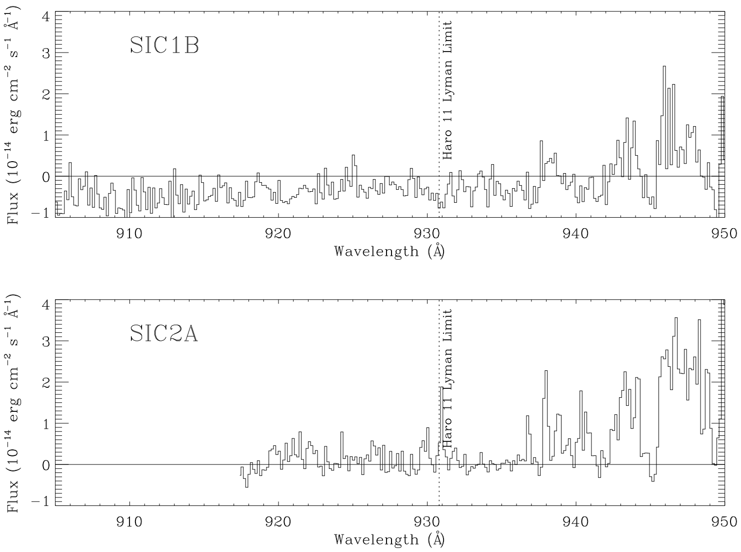

Fig. 7.— SiC 1B and SiC 2A night spectra (binned by 12 pixels=0.156 Å) of the Lyman continuum region. Both spectra have been run through the standard *FUSE* data pipeline. The SiC 1B background has clearly been oversubtracted in this wavelength region resulting in a negative flux.

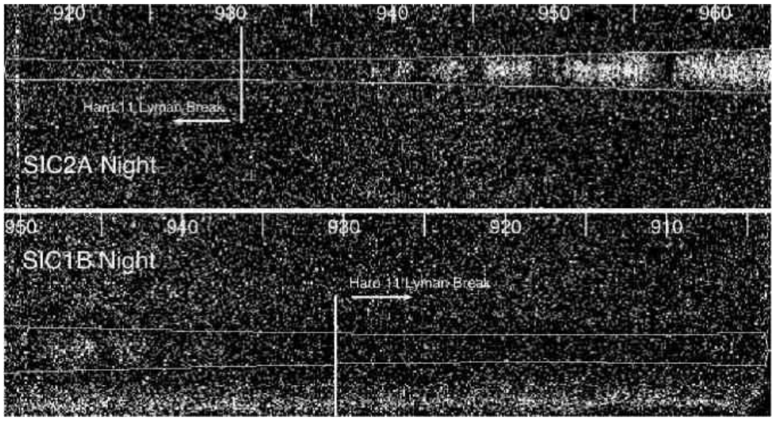

Fig. 8.— SiC 1B and SiC 2A image of the detectors in the Lyman continuum region during orbital night. The point source extraction aperture has been overlayed for both detectors. No clear emission can be seen in the Lyman continuum region on either detector. Background subtraction of the SiC 1B spectra is complicated by its location near the lower edge of the detector. Vertical structure in the background can also been seen on both detectors.

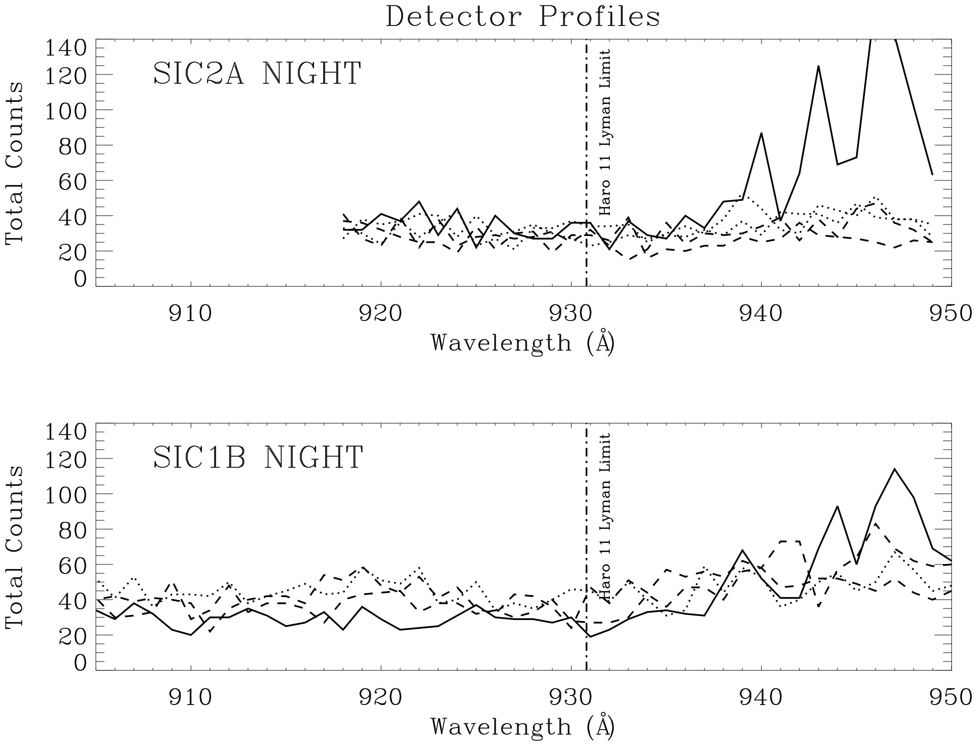

Fig. 9.— We have extracted the number of counts in 1Å bins from a rectangular region enclosing the source aperture (black line) and background regions directly below (dotted) and directly above (dashed) the aperture. The background profiles are very similar to the source profile below the Lyman limit. At variance with Bergvall et al. (2006) there does not appear to be any excess counts in the source regions below the Lyman limit. Note that several Lyman series absorption lines are visible above the Lyman limit. These profiles are consistent with a visual analysis of the 2-D spectra shown in Figure 8.

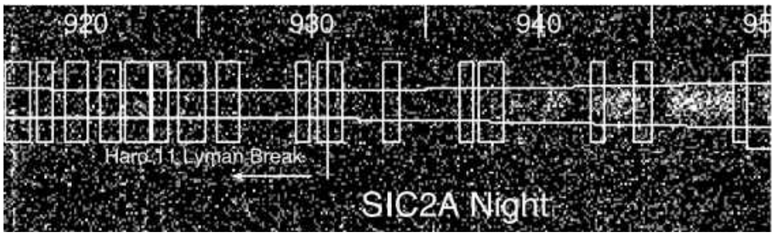

Fig. 10.— SiC 2A night image of the detector with the SiC 2A airglow regions identified by CalFUSE 3.1.8.

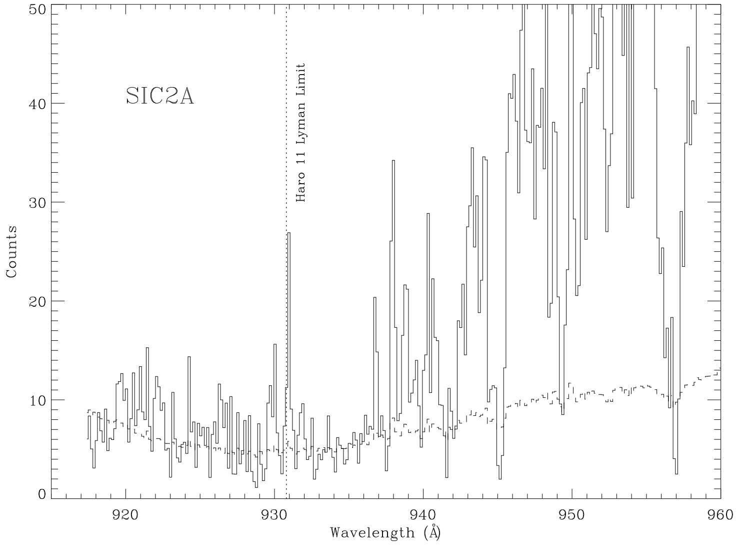

Fig. 11.— Total counts (spectra + background) from optimal extraction (binned by 12 pixels=0.156 Å) in the SiC 2A night time observation as a function of wavelength. The fitted background is shown as a dashed line. This plot again shows that the background dominates any signal in the Lyman continuum region.

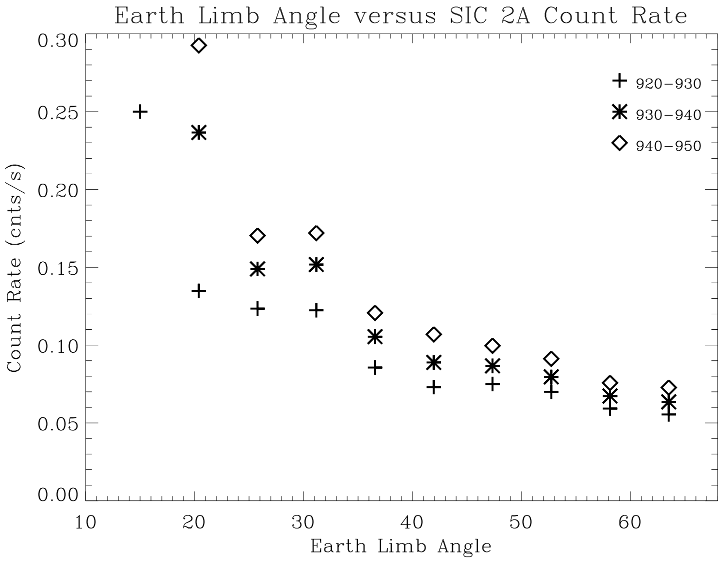

Fig. 12.— This plot shows the count rate in three wavelength regions of the LWRS aperture for the SiC 2A detector as a function of earth limb angle. The 920-930 Å bandpass, which represents the Lyman continuum emission region, has the lowest count rate for all limb angles and appears to still be falling at the highest angles. The expected intrinsic count rate of the detector from cosmic rays and ^{40}K decays is ~ 0.05 counts s^{-1} which is just below the count rate seen at the highest earth limb angles. This suggests that any excess emission in the SiC 2A spectra below the Lyman limit can be attributed to airglow.

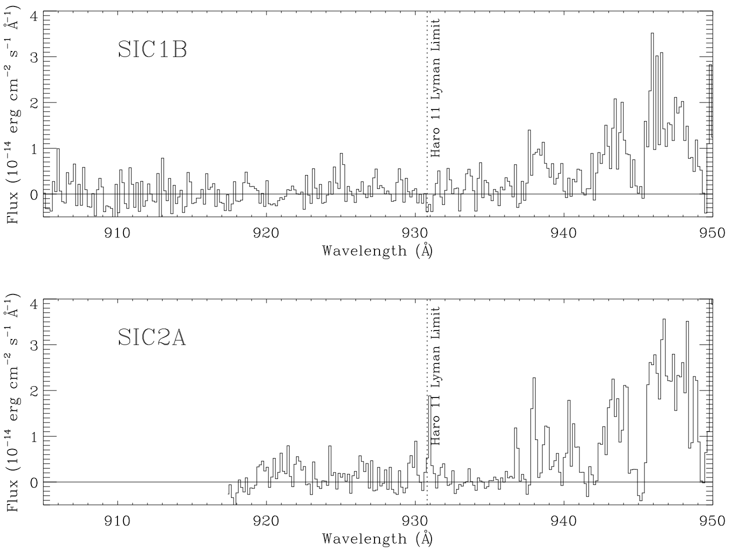

Fig. 13.— SiC 1B and SiC 2A night spectra (binned by 12 pixels=0.156 Å) of the Lyman continuum region. The background subtraction of the SiC 1B spectrum has been adjusted to match a flux level similar to that in the SiC 2A spectrum. Neither spectra show convincing evidence of Lyman continuum emission. In particular it should be noted that apparent features in one spectra are not replicated in the other as expected in noisy, low S/N spectra.

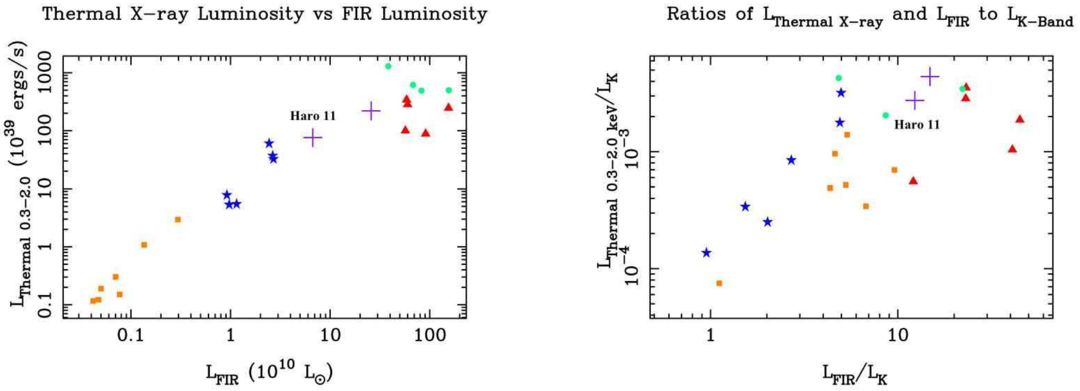

Fig. 14.— These plots are originally described in Grimes et al. (2005). The left Figure shows a relationship between $L_{\rm FIR}$ (SFR) and the thermal X-ray luminosity (0.3-2.0 keV). On the right we have divided both the thermal X-ray and the FIR luminosity by the *K*-band luminosity (a proxy for stellar mass). The FIR luminosity of the dwarf starbursts is actually the sum of the their UV and FIR luminosities. There is a clear linear relation between the SFR per stellar mass and the thermal X-ray emission per stellar mass. The IRAS and *K*-band data were obtained from *NED* and have been tranformed using the methods of Sanders & Mirabel (1996) and Carpenter (2001) respectively. Both VV 114 and Haro 11 follow the scaling relation defined by starbursts. Symbols indicate dwarf starbursts (orange squares), starbursts (blue stars), ULIRGs (red triangles), AGN ULIRGs (green circles), and local LBG analogues (purple crosses).

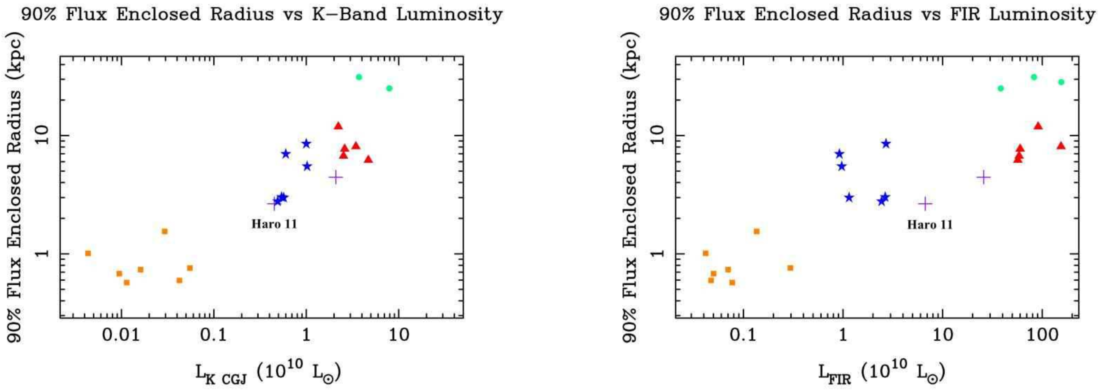

Fig. 15.— 90% flux enclosed radii in the 0.3-1.0 keV X-ray band vs K-band and FIR luminosity (see Grimes et al. (2005) for details). The size of the X-ray emitting region is correlated with the stellar mass (K-band) and SFR (FIR). The FIR luminosity of the dwarf starbursts is actually the sum of the their UV and FIR luminosities. The LBG analogues (VV 114 and Haro 11) fall on the low end of FIR relation due to their high SFR and compact size. The spatial extent of the hot X-ray gas appears to be more strongly correlated with the mass of the host galaxy. Symbols indicate dwarf starbursts (orange squares), starbursts (blue stars), ULIRGs (red triangles), AGN ULIRGs (green circles), and local LBG analogues (purple crosses).

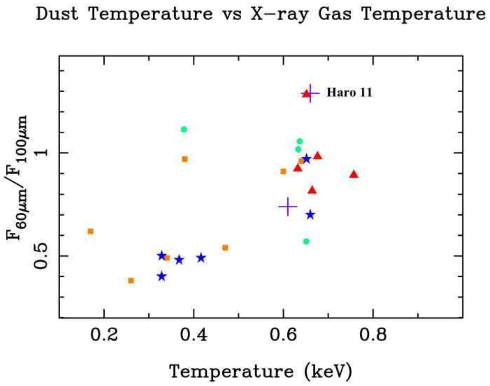

Fig. 16.— $F_{60\mu m}/F_{100\mu m}$ vs X-ray gas temperature. The $F_{60\mu m}/F_{100\mu m}$ ratio is an indicator of dust temperature and hence the SFR per unit area. There is a rough correspondence between the gas and dust temperatures. While VV 114 falls near the principal relation, Haro 11 is an outlier with F60μm/F100μm=1.29. Symbols indicate dwarf starbursts (orange squares), starbursts (blue stars), ULIRGs (red triangles), AGN ULIRGs (green circles), and local LBG analogues (purple crosses).